Optimization of Hybrid Organic–Inorganic Interdigitated Photovoltaic Device Structure Using a 2D Diffusion Model

Emiljana Krali[†] and Richard J. Curry[‡,*]

[†]Optical and Semiconductor Devices Group, Department of Electrical and Electronic Engineering, Imperial College, London SW7 2AZ, U.K., and
[‡]Advanced Technology Institute, University of Surrey, Guildford, Surrey, GU2 7XH, U.K.

ABSTRACT To improve the efficiency of organic photovoltaic devices the inclusion of semiconducting nanoparticles such as PbS has been used to enhance near-infrared absorption. Additionally the use of interdigitated heterojunctions has been explored as a means of improving charge extraction. In this paper we provide a two-dimensional model taking into account these approaches with the aim of predicting an optimized device geometry to maximize the efficiency. The steady-state exciton population has been calculated in each of the active regions taking into account the full optical response based on using a finite difference approach to obtain approximate numerical solutions to the 2D exciton diffusion equation. On the basis of this we calculate the contribution of each active material to the device short circuit current and power conversion efficiency. We show that optimized structures can lead to power conversions efficiencies of ~50% compared to a maximum of ~17% for planar heterojunction devices. To achieve this the interdigitated region thickness should be ~800 nm with PbS and C_{60} widths of ~60 and 20 nm, respectively. Even modest nanopatterning using much thinner active regions provides improvements in efficiency and may be approached using a variety of methods including nanoimprinting lithography, nanotemplating, or the incorporation of presynthesized nanorod structures.

KEYWORDS: photovoltaic · device architecture · nanocrystal · fullerene · nanopatterning · efficiency · 2D diffusion · modeling

Intense research into organic and polymer photovoltaic devices (OPVs) has been undertaken in recent decades aimed at providing a low-cost and efficient means of solar energy conversion to satisfy the significant emerging renewable energy market.[1] While progress toward this goal continues, reported efficiencies remain below that required to compete with established inorganic photovoltaic technologies.[2] The factors that determine the external quantum efficiency η_{EQE} of OPV devices can be readily identified and summarized[3] as

$$\eta_{EQE}(\lambda) = \eta_A(\lambda)\,\eta_{ED}\eta_{CT}\eta_{CC} \qquad (1)$$

where η_A is the exciton generation (absorption) efficiency at wavelength λ; η_{ED} is the exciton diffusion efficiency to a disassociation site at a heterojunction; η_{CT} is the exciton disassociation efficiency at the heterojunction; and η_{CC} is the resulting efficiency of charge collection . In the case of OPV systems it is possible to choose materials such that the relative alignment of electronic energy levels at the heterojunctions results in $\eta_{CT} = 1$. As a result optimization of OPV device architectures has focused on maximizing the remaining efficiency parameters. Of these the relationship between $\eta_A(\lambda)$ and η_{ED} places a fundamental constraint on the design of OPV devices. To maximize absorption the active region of the OPV device should absorb all photons with energy above the constituent materials bandgap E_g. This thickness can be easily obtained *via* measurement of the absorption coefficient, $\alpha(\lambda)$, and modeling of the optical density within this region under AM1.5 irradiance. Furthermore, the E_g of the chosen active materials should also take into account the available solar spectrum, which extends into the near-infrared (NIR), and also take into account the relationship between E_g and the electronic properties of the device.[4] In general the majority of OPV devices are restricted to absorbing in the visible region of the solar spectrum, thus a significant proportion of the available solar spectrum is not utilized. To address this a number of hybrid organic–inorganic nanocrystal (NCs) devices have been reported in which NIR light is absorbed by the NCs resulting in a photocurrent and increasing $\eta_A(\lambda)$.[5−9]

To maximize η_{ED} it is found that the exciton generation site must be within a distance defined by the exciton diffusion length L_D of a heterojunction at which the exciton may disassociate.[10] For the materials used in OPV devices typically $L_D < 50$ nm; hence, this is the limiting factor in designing device architecture.

* Address correspondence to r.j.curry@surrey.ac.uk.

Received for review January 18, 2011 and accepted March 22, 2011.

Published online March 22, 2011
10.1021/nn200197f

As a result two OPV device configurations are commonly reported experimentally.[11] The first of these is a planar structure in which active materials are sequentially deposited on a transparent electrode to form the heterojunctions prior to a top electrode being deposited. For bilayer structures this has the advantage of ensuring a direct continuous pathway through each material for charge extraction following disassociation at the heterojunction, minimizing the potential to lose the charge carrier, with the disadvantage that the maximum thickness of each active layer is governed by its L_D. To overcome this a second device structure is often employed in which the active region consists of a blend of the two materials that together form the heterojunctions. In such blends (often referred to as bulk heterojunctions devices) the mixing and subsequent phase segregation of the materials results in a heterojunction being found within L_D of any point within the film. This allows much thicker films to be used, thus in principle enabling both $\eta_A(\lambda)$ and η_{ED} to be maximized. The significant disadvantage of this approach is that the blended films do not provide a direct pathway for charge extraction but rather a percolation pathway. Additionally, in this percolation process opposite charge carriers are likely to meet and recombine resulting in a reduction of the η_{CC} and therefore the $\eta_{EQE}(\lambda)$.

To resolve such issues a modified version of the bilayer device architecture has been proposed in which an interdigitated structure forms the heterojunction. In such a device the active layer thickness in the direction of light incidence may be extended while maintaining both the condition of having a heterojunction within each materials L_D and of providing a direct pathway for charge extraction which does not reduce η_{CC}. It is therefore of significant interest to develop an understanding of the optimal parameters of such a structure based on materials used in OPV devices and ascertain their experimental feasibility given the advances that continue to be made in nanoscale patterning, nanotemplating, and synthesis of nanorod structures. It is also important to determine the potential improvement in device performance if the optimized structure could be realized. Previously such structures have been proposed and modeled on the basis of devices in which only one active material is present[12] or both a donor and acceptor are assumed to absorb under monochromatic irradiation.[13] In both these cases 2D diffusion of excitons was considered, expanding on the 1D treatment previously reported that included optical interference within the device.[14] While extending the studies to include 2D diffusion of excitons, the simplification of using monochromatic irradiance and therefore absorption reduces the information that can be gained from the models and strongly influences the conclusions reached. This is particularly the case where two optically active materials form the device each with a different absorption spectrum.

In this paper we apply a 2D exciton diffusion model to predict the optimal interdigitated structure of hybrid organic–inorganic C_{60}–PbS NC photovoltaic devices. The model is generic to all heterojunction-forming materials systems used in OPV devices. The PbS NC materials system is chosen to allow the impact of utilizing the NIR spectral region on efficiency to also be studied. In doing so the model takes into account the full wavelength dependency of the photocurrent generation in each of the active materials which extends into the NIR for the PbS NCs. We obtain the optimal device design and based on this an upper limit to the efficiency of such devices in comparison to that of simple planar architectures reported to date. It is shown that the use of interdigitated structures can lead to a 3-fold increase in the efficiency, and the results are discussed in relation to experimental devices based on these materials and advances in nanopatterning within OPV devices.

RESULTS

We first consider the planar device architecture in which the optical intensity at any given point x within each layer is determined based on the Beer–Lambert relation and is given by (Supporting Information):

$$I_1(x,\lambda) = I_0(\lambda)\, T_{ITO}(\lambda) \left[e^{-\alpha_1(\lambda)x} + e^{-2\alpha_1(\lambda)d_1} e^{-2\alpha_2(\lambda)d_2} e^{\alpha_1(\lambda)x}\right] \quad (2)$$

and

$$I_2(x,\lambda) = I_0(\lambda)\, T_{ITO}(\lambda) e^{-\alpha_1(\lambda)d_1} \left[e^{-\alpha_2(\lambda)x} + e^{-2\alpha_2(\lambda)d_2} e^{\alpha_2(\lambda)x}\right] \quad (3)$$

for layers 1 and 2, respectively, where for each layer $x = 0$ is defined as being at the bottom boundary with light entering layer 1 first through the ITO substrate. Schematics of the device architectures considered are provided in Figure 1a. In keeping with the design of experimentally reported devices, we consider the case of PbS forming layer one and C_{60} layer two despite PbS having the narrower bandgap. Modeling the light intensity within the device by solving Maxwell's equations would add considerable complexity to the treatment as we consider variation of both layer thicknesses with each layer having considerable absorption in the visible region (Figure 1b). Additionally, we consider the full wavelength dependency in our model which again would further complicate our treatment. As such this type of treatment is left for future development.

Multiplication of eqs 2 and 3 with the absorption coefficient of the respective materials and taking into account the energy of the incident photons yields the exciton generation terms:

$$G_{ex,1}(x,\lambda) = \frac{\lambda}{hc}\alpha_1(\lambda) I_0(\lambda)\, T_{ITO}(\lambda) \left[e^{-\alpha_1(\lambda)x} + e^{-2\alpha_1(\lambda)d_1} e^{-2\alpha_2(\lambda)d_2} e^{\alpha_1(\lambda)x}\right] \quad (4)$$

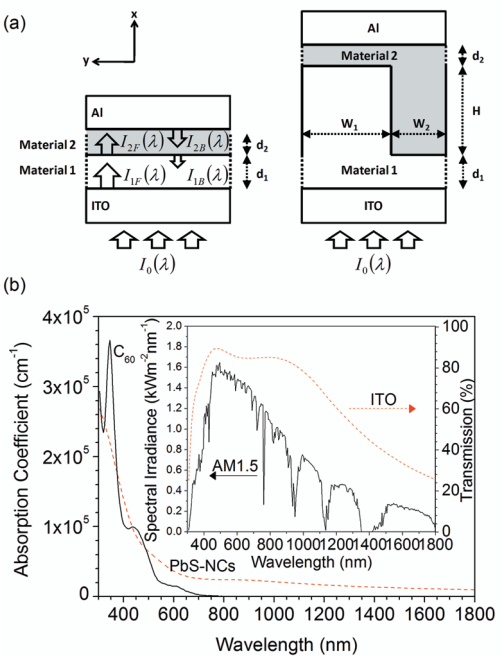

Figure 1. Schematic of the planar and interdigitated device architectures modeled (a) and the absorption spectra of PbS NC and C_{60} with the AM1.5 and ITO transmission spectra inset (b). In this study materials 1 and 2 are PbS NCs and C_{60}, respectively.

$$G_{ex,2}(x,\lambda) = \frac{\lambda}{hc}\alpha_2(\lambda)I_0(\lambda)\,T_{ITO}(\lambda)e^{-\alpha_1(\lambda)d_1} [e^{-\alpha_2(\lambda)x} + e^{-2\alpha_2(\lambda)d_2}e^{\alpha_2(\lambda)x}] \quad (5)$$

In eqs 4 and 5 we assume that each absorbed photon yields an exciton at that point within the structure. To apply these expressions to the interdigitated structures the total thickness of each film must be used which changes periodically along the y-direction.

To obtain the exciton density per unit wavelength within the planar devices we use a 1D continuity expression[15] given as

$$\frac{\partial n_{ex,i}(x,t,\lambda)}{\partial t} = D_{ex,i}\frac{\partial^2 n_{ex,i}(x,t,\lambda)}{\partial x^2} - \frac{n_{ex,i}(x,t,\lambda)}{\tau_{ex,i}} + G_{ex,i}(x,\lambda) \quad (6)$$

where $D_{ex,i} = L_i^2/\tau_{ex,i}$ is the exciton diffusion coefficient, L_i and $\tau_{ex,i}$ are the exciton diffusion length and lifetime, respectively, and $n_{ex,i}(x,t,\lambda)$ is the exciton density in layer i. The three terms on the right of eq 6 represent the exciton diffusion, recombination, and generation, respectively. We consider the exciton population in steady state, hence $\partial n_{ex,i}(x,t,\lambda)/\partial t = 0$, and we can then rewrite eq 6 as

$$\frac{d^2 n_{ex,i}(x,\lambda)}{dx^2} = \beta_i^2 n_{ex,i}(x,\lambda) - \frac{G_{ex,i}(x,\lambda)}{D_{ex,i}} \quad (7)$$

where $\beta_i = 1/(D_{ex,i}\tau_{ex,i})^{1/2}$. To obtain solutions to eq 7 we assume that excitons are quenched with 100% efficiency at both the heterojunction and electrode interfaces thus $(n_{ex,i}(0,\lambda)) = n_{ex,i}(d_i,\lambda) = 0$. This is supported by experimental observations and results in $\eta_{CT} = 1$ as discussed above.

The solution to eq 7 is given by

$$n_{ex,i}(x,\lambda) = \frac{\lambda I_0 T_{ITO}(\lambda)\,\alpha_i(\lambda)\,b_i(\lambda)}{hcD_{ex,i}(\beta_i^2 - \alpha_i^2(\lambda))} [e^{-\alpha_i(\lambda)x} + c_i(\lambda)\,e^{\alpha_i(\lambda)x}] + A_i(\lambda)\,e^{\beta_i x} + B_i(\lambda)\,e^{-\beta_i x} \quad (8)$$

where

$$A_i(\lambda) = \frac{\lambda I_0 T_{ITO}(\lambda)\,\alpha_i(\lambda)\,b_i(\lambda)}{hcD_{ex,i}(\beta_i^2 - \alpha_i^2(\lambda))(1 - e^{2\beta_i d_i})} [(e^{[\beta_i - \alpha_i(\lambda)]d_i} - 1) + c_i(\lambda)\,(e^{[\beta_i + \alpha_i(\lambda)]d_i} - 1)] \quad (9)$$

$$B_i(\lambda) = \frac{\lambda I_0 T_{ITO}(\lambda)\,\alpha_i(\lambda)\,b_i(\lambda)}{hcD_{ex,i}(\beta_i^2 - \alpha_i^2(\lambda))(1 - e^{2\beta_i d_i})} [(e^{-[\beta_i + \alpha_i(\lambda)]d_i} - 1) + c_i(\lambda)\,(e^{-[\beta_i - \alpha_i(\lambda)]d_i} - 1)] \quad (10)$$

and $b_1(\lambda) = 1$, $b_2(\lambda) = e^{-\alpha_1 d_1}$, $c_1(\lambda) = e^{-2\alpha_1 d_1}e^{-2\alpha_2 d_2}$, and $c_2(\lambda) = e^{-2\alpha_2 d_2}$.

At the heterojunction we can write the exciton current density as

$$J_{ex}(\lambda) = -D_{ex,1}\left(\frac{dn_{ex,1}(x,\lambda)}{dx}\right)_{x=d_1} + D_{ex,2}\left(\frac{dn_{ex,2}(x,\lambda)}{dx}\right)_{x=0} \quad (11)$$

which is related to the short circuit photocurrent by

$$J_{sc}(\lambda) = q\eta_{CT}J_{ex}(\lambda) \quad (12)$$

where q is a unit charge and we assume $\eta_{CT} = 1$. Finally, we obtain the wavelength dependent external quantum efficiency as

$$\eta_{EQE}(\lambda) = \frac{hcJ_{sc}(\lambda)}{q\lambda I_0(\lambda)} \quad (13)$$

To obtain the total exciton density we integrate eq 8 with respect to λ and likewise eq 12 to obtain the total short circuit current. The average external quantum efficiency is given by

$$\overline{\eta}_{EQE} = \frac{\int_{\lambda_{min}}^{\lambda_{max}} \lambda I_0(\lambda)\,\eta_{EQE}(\lambda)\,d\lambda}{\int_{\lambda_{min}}^{\lambda_{max}} \lambda I_0(\lambda)\,d\lambda} \quad (14)$$

For comparison we also calculate $\eta_{EQE}(\lambda)$ and $\overline{\eta}_{EQE}$ from $\eta_{EQE,i}(\lambda) = \eta_{A,i}(\lambda)\,\eta_{ED,i}$ using the expressions $\eta_{A,i}(\lambda) = 1 - e^{-\alpha_i(\lambda)d_i}$ and $\eta_{ED,i} = e^{-d_i/L_i}$ as previously reported.[7]

Figure 2 shows $\overline{\eta}_{EQE}$ as a function of both PbS NC and C_{60} film thickness obtained without and by solving the 1D diffusion model (Figure 2 panels a and b, respectively). An exciton diffusion length of 40 nm was used for C_{60} based on previous reports.[3] A larger

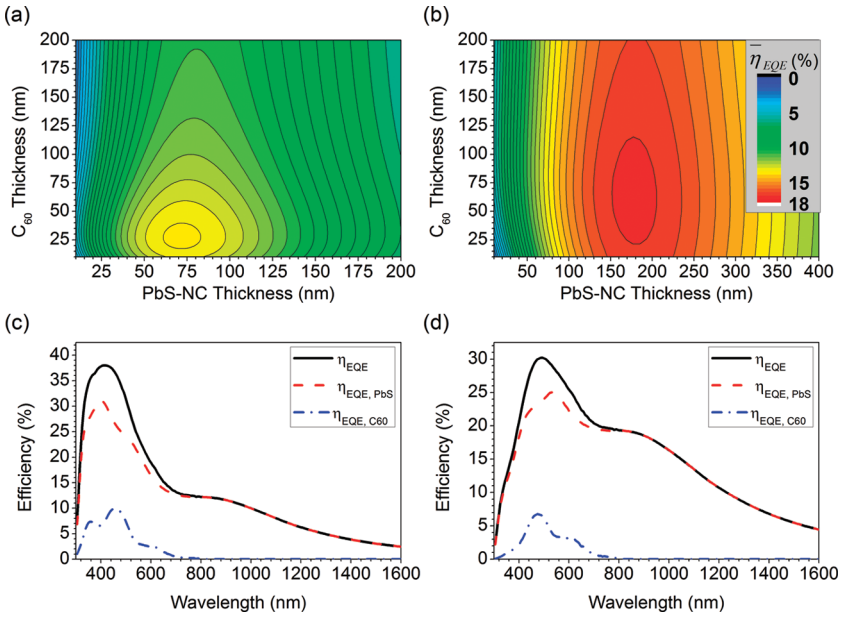

Figure 2. $\bar{\eta}_{EQE}$ as a function of PbS NC and C_{60} thickness obtained from modeling the planar heterojunction device without (a) and with (b) solving the 1D exciton diffusion equation. Panels c and d show $\eta_{EQE}(\lambda)$ calculated using the optimum PbS NC and C_{60} values indicating the contribution of each layer obtained from panels a and b, respectively. Panel a is plotted using the same scale for $\bar{\eta}_{EQE}$ as indicated in inset b.

exciton diffusion length of 100 nm was used for the PbS NC based on that estimated for similar PbSe NCs.[16] It can be observed that $\bar{\eta}_{EQE}$ is more sensitive to the PbS NC thickness than that of C_{60} in both models. This is due to the significant contribution of PbS NCs to the photocurrent in both the visible and the NIR region in comparison to C_{60} as can be seen in Figure 2c,d. Such behavior is not unreasonable and could be inferred from the absorption spectra in Figure 1b. When comparing the maximum values of $\bar{\eta}_{EQE}$ and corresponding $\eta_{EQE}(\lambda)$ for each model, it is noticeable that the predicted $\bar{\eta}_{EQE}$ is higher when the 1D diffusion equation is solved (17.2% compared with 13.7%) despite having a lower maximum value of $\eta_{EQE}(\lambda)$ in comparison when 1D diffusion is not included. This is accounted for by an increase in the predicted performance in the NIR in the diffusion model.

Of more significance is the predicted optimal layer thicknesses obtained from the two models. If 1D exciton diffusion is not included then an optimal PbS NC thickness of ~68 nm (±10 nm) is predicted in comparison to ~174 nm (±25 nm) when such diffusion is considered. This 3-fold increase is not only beneficial in terms of light absorption but also in relation to device manufacture where these thicker films are easier to deposit. Additionally the increase in tolerance will also reduce the susceptibility to significant variation in performance due to small fluctuations in layer thicknesses between devices. The above-mentioned dominance of the PbS NC layer on $\bar{\eta}_{EQE}$ also results in a significant increase in the tolerance of device performance in relation to the C_{60} layer thickness. As for the PbS NCs the consideration of 1D exciton diffusion

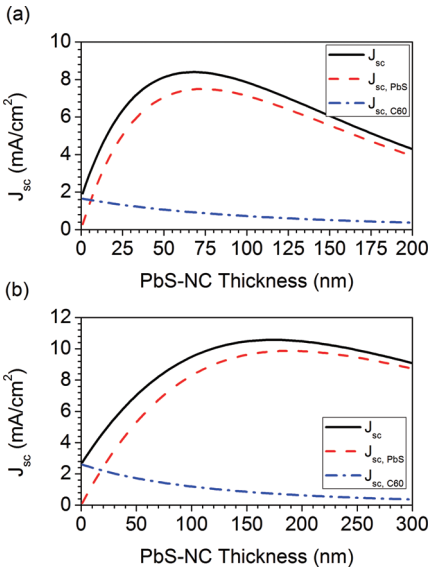

Figure 3. J_{sc} *vs* PbS NC thickness obtained from modeling the planar heterojunction device without (a) and with (b) solving of the 1D exciton diffusion equation.

increases the optimal C_{60} layer thickness from ~23 nm (±10 nm) to ~61 nm (±25 nm), Figure 2a,b. It is of interest to note that very thin (~10 nm) C_{60} films may be used with only a small decrease in the overall device $\bar{\eta}_{EQE}$. This is in line with previous reports of PbSe NC devices in which the NCs act as the only photoactive layer either in a Schottky device between metal electrodes[16,17] or in conjunction with electron and hole extraction layers.[18]

Figure 3 panels a and b show the predicted total short circuit current, J_{SC}, from the two models,

obtained by integration of eq 12, as a function of PbS NC layer thickness for the optimum C_{60} layer thickness determined from the maximum $\overline{\eta}_{EQE}$. This clearly demonstrates the importance of using the full diffusion equation approach to model the performance of these devices and guide their future design. Though the increase in J_{SC} predicted by the diffusion model is modest, it shows that a device fabricated using the PbS NC thickness in the simpler model will only yield ~50% of the potential photocurrent. Furthermore, the performance of such a device is much more susceptible to variations in the layer thickness due to the higher degree of curvature.

To model the performance of the interdigitated device structure shown in Figure 1a, we divide the repeating unit into two vertical components of thickness w_1 and w_2. Because of the assumed normal incidence of light, intensity and exciton generation terms within each layer of the two units are obtained as for the 1D model (eqs 2−5). We consider exciton diffusion in both the *x*- and *y*-direction; thus under steady-state conditions eq 6 is rewritten as

$$D_{ex}\left(\frac{\partial^2 n_{ex}(x,y,\lambda)}{\partial x^2}+\frac{\partial^2 n_{ex}(x,y,\lambda)}{\partial y^2}\right)-\frac{n_{ex}(x,y,\lambda)}{\tau_{ex}}+G_{ex}(x,y,\lambda)=0 \quad (15)$$

where we have dropped the subscript previously used to explicitly identify the layer. In solving eq 15 we again use the boundary conditions that exciton disassociation occurs with unit efficiency at heterojunction interfaces and the electrodes, while between repeating units of identical material the solution must be periodic. To obtain a solution to eq 15 we use the finite difference method[19] applied in turn to each "L"-shaped repeating unit dividing each unit into a discrete mesh defined by points given as (x_j,y_i) with $j = 0, ..., N$ and $i = 0, ..., M$ representing the subdivisions in the *x*- and *y*-directions, respectively. To aid clarity we define $u_{ji} = n_{ex}(x_j,y_i,\lambda)$ and may write the partial derivative terms in eq 15 as

$$\frac{\partial^2 u}{\partial x^2}=\frac{u_{(j+1)i}-2u_{ji}+u_{(j-1)i}}{h^2}+\vartheta(h^2) \quad (16)$$

and

$$\frac{\partial^2 u}{\partial y^2}=\frac{u_{j(i+1)}-2u_{ji}+u_{j(i-1)}}{k^2}+\vartheta(k^2) \quad (17)$$

where h and k are the increments in the *x*- and *y*-direction, respectively, and $\vartheta(h^2)$ and $\vartheta(k^2)$ indicate accuracy to second-order in comparison with the true derivatives. Substitution of eqs 16 and 17 into eq 15 yields

$$a_{ji}u_{(j-1)i}+b_{ji}u_{j(i-1)}-c_{ji}u_{ji}+b_{ji}u_{j(i+1)}+a_{ji}u_{(j+1)i}=-s_{ji} \quad (18)$$

where $a_{ji} = D_{ex,ji}/h^2$, $b_{ji} = D_{ex,ji}/k^2$, $c_{ji} = 2D_{ex,ji}/h^2 + 2D_{ex,ji}/k^2 + 1/\tau_{ex,ji}$ and $s_{ji} = G_{ex,ji}(x,y,\lambda)$. Equation 18 is only valid at internal mesh points and must be modified at the boundaries according to the boundary conditions (Supporting Information). Finite difference approximate solutions were subsequently obtained allowing the exciton density to be determined within each "L"-shaped unit for a given monochromatic incident intensity and the total number of excitons reaching the heterojunction. From this the $\eta_{EQE}(\lambda)$ was then obtained.

As a starting point for determining the optimum interdigitated geometry we turn to the results obtained from planar structures using the 1D diffusion model. The widths of the PbS NC and C_{60} in the interdigitated region, w_1 and w_2, respectively (Figure 1a), are initially set to the optimum thicknesses obtained as discussed above (w_1 = 170 nm and w_2 = 60 nm). Similarly we also set the continuous C_{60} film thickness adjacent to the electrode as $d_2 = 60$ nm. In considering the thickness of the continuous PbS NC layer, d_1, setting this to 170 nm would result in the height of the interdigitated region, H, having to be rather small if it were assumed that the combined thickness of $d_1 + H$ should be around the optimum value of ~170 nm. We therefore initially choose to set H = 100 nm and d_1 = 50 nm. With the use of these values, the exciton population distribution under steady-state conditions, $n_{ex}(x_j,y_i,\lambda)$, may be obtained as a function of wavelength within the device .

We plot in Figure 4 $n_{ex}(x_j,y_i,\lambda)$ at 400, 500, and 600 nm corresponding to the product of $\alpha_i(\lambda)(d_i + H)$ having a value of ~2, ~1, and ~0.5 for PbS NC and ~1.7, ~0.9, and ~0.24 for C_{60} for these initial values of H, d_i, and w_i. Also shown in Figure 4d is $n_{ex}(x_j,y_i,\lambda)$ calculated at λ = 1000 nm showing the exciton distribution due to NIR absorption within the PbS NC layer. Within the PbS NC layer the maximum exciton population for values of $\alpha_i(\lambda)(d_i + H) \leq 1$ is found to be located in a similar position, even for long wavelengths, and only moves slightly toward the front (ITO electrode) of the device for higher values. This is significant as it implies that the PbS NC layer geometry can be adjusted to optimize device performance across the entire optical region. Within the C_{60} layer it can be seen that as $\alpha_i(\lambda)(d_i + H)$ is decreased the position of the maximum exciton population moves toward the rear (Al electrode) of the device and is therefore more susceptible to changes in the layer geometry. For both layers the position of the electrode and heterojunction interface also strongly influence the position of maximum $n_{ex}(x_j,y_i,\lambda)$ *via* the boundary conditions used.

In Figure 5a we show $n_{ex}(x_j,y_i)$ obtained by integrating over all wavelengths. Immediately evident in all these figures is the significantly lower value of $n_{ex}(x_j, y_i,\lambda)$ in the C_{60} region in comparison to the PbS NC region. At 500 nm the maximum value of $n_{ex}(x_j,y_i,$

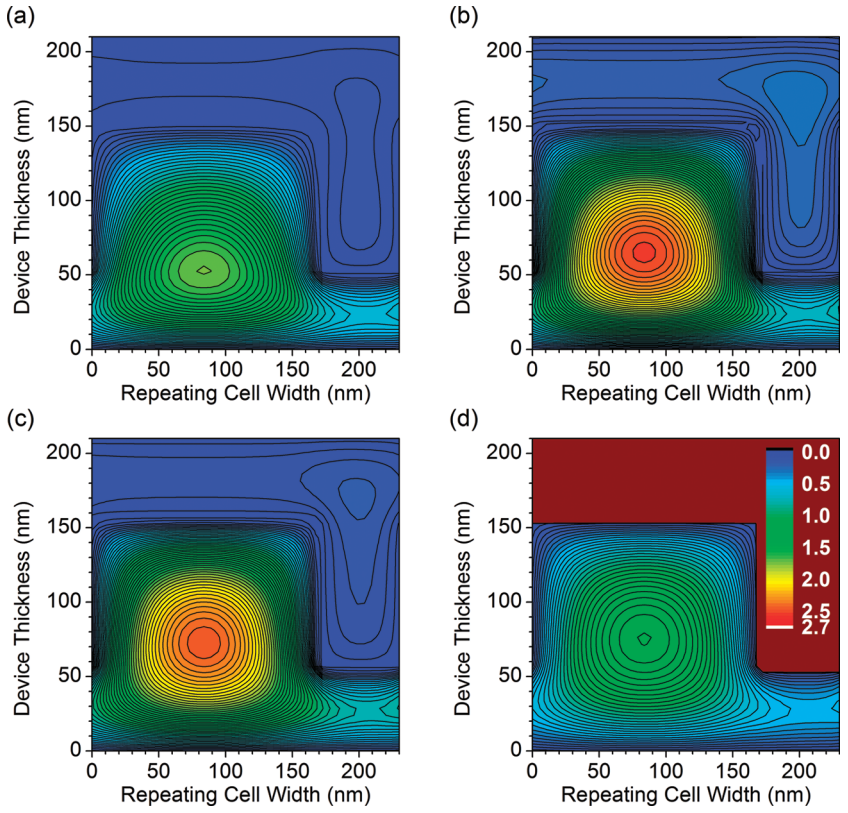

Figure 4. Steady-state exciton population, $n_{ex}(x_j,y_i,\lambda)$, calculated at 400 (a), 500 (b), 600 (c) and 1000 nm (d). The scale inset to panel d also applies to panels a−c.

500 nm) is 2.57 and 0.35 in the PbS NC and C_{60} region, respectively. Integrating over all wavelengths naturally increases this difference due to the extended absorption of the PbS NC leading to a ~2 orders of magnitude difference between the PbS NC ($n_{ex}(x_j,y_i)^{PbS}_{max} \approx 1600$) and C_{60} ($n_{ex}(x_j,y_i)^{C60}_{max} \approx 60$). However, the significant difference between these values does not translate into a similar variation in the contribution to the device efficiency. For example the values of η_{EQE}(500 nm) from each region are in the ratio of 2:1 respectively, Figure 5b. This exciton distribution within each layer reflects that observed in Figure 4 with the notable effect that a much more uniform distribution is found in the C_{60} layer. Even though the maximum values of $n_{ex}(x_j,y_i)$ naturally occur at the furthest point from the heterojunction and hence a direct correspondence with $\eta_{EQE}(\lambda)$ might not be expected, this does imply that improvement in device efficiency can be achieved *via* optimization of the device parameters.

To study this, we sequentially varied the values of w_1, w_2, and H leaving d_1 and d_2 fixed at the values described above. Increasing H leads to an increase in the path length for absorption and, with our assumption of perfect charge collection, will provide an improvement in $\overline{\eta}_{EQE}$. This is demonstrated in Figure 6a which shows $\overline{\eta}_{EQE}$ increasing to a maximum value which occurs upon absorption of all incident photons within the device. However, obtaining such values of H experimentally would be difficult, and also the device would become limited by the charge extraction efficiency in practice. As a result, when considering the parameters w_1 and w_2 we fix H = 1000 nm which is at the upper limits of what might be experimentally achieved and above which little further improvement in $\overline{\eta}_{EQE}$ is obtained. Initially varying w_1, we observe that values in the region of ~85 nm to ~170 nm provide the most efficient devices with $\overline{\eta}_{EQE}$ = 42% at H = 1000 nm in keeping with the PbS NC exciton diffusion length (100 nm) used in the study (Figure 6a). A closer study of the value of w_1 within this range is provided in Figure 6b showing that $\overline{\eta}_{EQE}$ is maximized at w_1 = 115 nm. Taking this value of w_1, we now vary w_2 to obtain a corresponding optimal value for maximizing $\overline{\eta}_{EQE}$. Unlike for w_1 we observe that $\overline{\eta}_{EQE}$ linearly increases with reducing w_2 even for values below the C_{60} exciton diffusion length, Figure 6b. This finding is similar to that obtained for the bilayer device structures discussed above (Figure 2b) in which very thin C_{60} films can be used without significant reduction in $\overline{\eta}_{EQE}$. Finally, we again vary w_1 while fixing w_2 and obtain optimal device performance with $\overline{\eta}_{EQE}$ = 50% even when H is reduced to 800 nm which is likely to improve charge extraction and be experimentally easier to fabricate, Figure 6b.

In Figure 7 we show $\eta_{EQE}(\lambda)$ for an optimized device with parameter values of w_1 = 60 nm, w_2 = 20 nm,

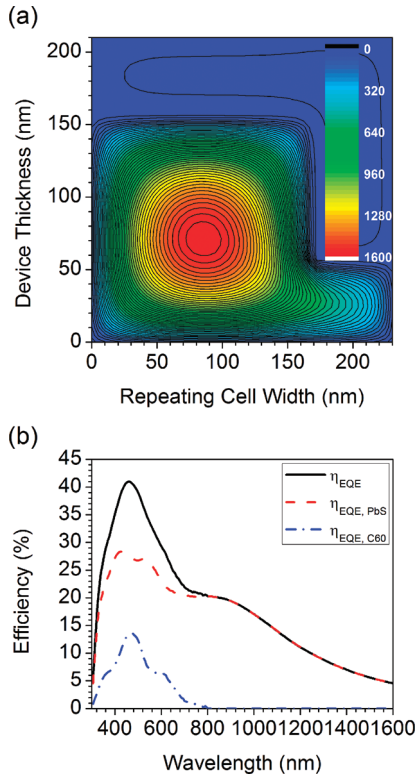

Figure 5. Steady-state exciton population $n_{ex}(x_i,y_i)$ (a) and $\eta_{EQE}(\lambda)$ showing the contribution from each region (b) for the device parameters $w_1 = 170$ nm, $w_2 = 60$ nm, $H = 100$ nm, $d_1 = 50$ nm, and $d_2 = 60$ nm.

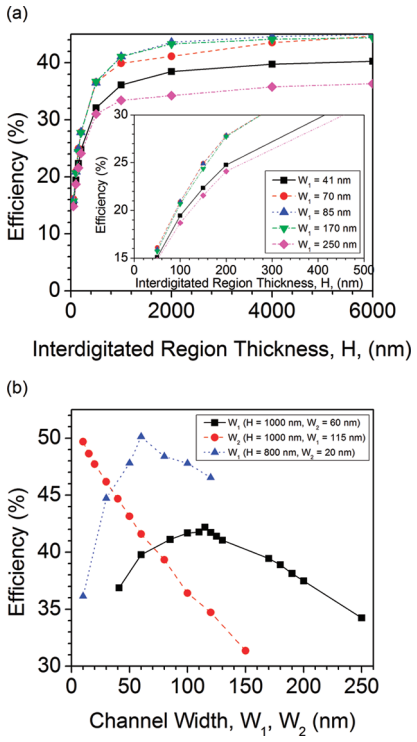

Figure 6. $\overline{\eta}_{EQE}$ as a function of interdigitated region thickness H and PbS NC channel width w_1 (a) and as a function of PbS NC and C_{60} channel widths w_1 and w_2 (b).

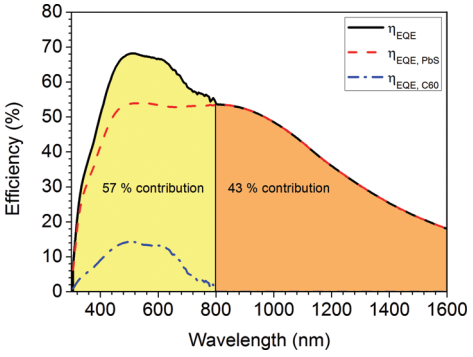

Figure 7. $\eta_{EQE}(\lambda)$ for an optimized device with parameter values of $w_1 = 60$ nm, $w_2 = 20$ nm, $H = 800$ nm, $d_1 = 50$ nm, and $d_2 = 60$ nm. The individual contributions from the C_{60} and PbS NCs are shown along with the total contribution to η_{EQE} of the spectral regions above and below 800 nm.

$H = 800$ nm, $d_1 = 50$ nm, and $d_2 = 60$ nm resulting in a value of $\overline{\eta}_{EQE} \approx 48\%$, close to the maximum predicted value of $\overline{\eta}_{EQE}$ in Figure 6b. While overall $\eta_{EQE}(\lambda)$ has been significantly improved, in comparison with Figure 5b, it can be seen that optimizing the device architecture has enhanced the NIR contribution with the result of broadening the spectrum. This is true for both materials, and though the peak C_{60} contribution to $\overline{\eta}_{EQE}$ has been reduced, its overall contribution has increased from 2.6% in Figure 5b to 4.3% in Figure 7. The increase in PbS NC contribution is more significant rising from ~17% in Figure 5b to ~44% in Figure 7.

We also show in Figure 7 the relative contribution to $\overline{\eta}_{EQE}$ provided by incident light above and below 800 nm. The high energy regime ($\lambda < 800$ nm) contributes most (57%) which if taken alone would result in a value of $\overline{\eta}_{EQE} = 27\%$. This demonstrates the generic importance of considering device architecture in all OPV systems. However, it is also clear that the NIR region is also significant and should be considered in future device optimization. This region ($\lambda > 800$ nm) makes a contribution of ~43% toward the total predicted value of $\overline{\eta}_{EQE}$.

DISCUSSION

In the above model the treatment of exciton diffusion significantly impacts on the predicted optimum device geometry in both the planar and interdigitated structures. In the planar devices the strongest effect is to reduce the importance of the C_{60} film thickness in determining efficiency. Despite this the presence of a thin film is still necessary to allow charge separation while also providing a contribution to $\overline{\eta}_{EQE}$. In relation to the critical parameters of photovoltaic devices, the presence of C_{60} and subsequent nature of the heterojunction determines the maximum open circuit voltage and therefore measured power conversion efficiency $\overline{\eta}_{EQE}^{Meas}$. The model based on 1D diffusion predicts optimal layer thicknesses of ~175 and ~60 nm for PbS NC and C_{60}, respectively. Devices reported to date based on a PbS NC/C_{60} heterojunction

have used PbS NC films *ca.* 100 nm[7] and 90 nm[9] in thickness. In the former a 30 nm thick C_{60} film was used, and the reported value of $\overline{\eta}_{EQE}^{Meas}$ = 0.44% was significantly below the maximum (15%, Figure 2b) predicted above for these thicknesses. More recently the effect of varying the C_{60} thickness over a small range (0−50 nm) was reported with a 90 nm thick PbS NC film.[9] These devices showed a maximum value of $\overline{\eta}_{EQE}^{Meas}$ = 2.2% with a 30 nm C_{60} layer which is attributed to significant improvement in charge carrier mobility through the PbS NC film following cross-linking with 1,3-benezendithiol, though again is still below what is predicted (14%, Figure 2b). The model predicts little variation (<1%) in $\overline{\eta}_{EQE}$ from this value as the C_{60} thickness is varied over the experimentally studied range. Experimentally, variation is observed increasing due to improved fill factor as the C_{60} thickness is increased from 10 to 30 nm. For the 50 nm thick C_{60} devices $\overline{\eta}_{EQE}^{Meas}$ is reduced, in contrast with the prediction from Figure 2b, though these devices have a notably reduced J_{sc} and increased series resistance. The reproducibility of the results presented was not discussed though the optical reflection studies reported indicate that the 50 nm C_{60} film device should further improve $\overline{\eta}_{EQE}^{Meas}$ in line with this study.

Given the value of $\overline{\eta}_{EQE}^{Meas}$ = 2.2% achieved in planar devices, it is of interest to discuss the potential benefits of patterning in relation to further improving this value. The 2D diffusion modeling of the interdigitated devices indicated that values up to $\overline{\eta}_{EQE}$ = 50% can be achieved *via* the use of patterning with the width of the PbS NC and C_{60} regions being ∼60 and 20 nm, respectively. Absorption in this case is optimized by allowing a ∼800 nm thick interdigitated region with planar PbS NC and C_{60} layers at the electrode interfaces 50 and 60 nm thick, respectively. The increase in $\overline{\eta}_{EQE}$ achieved by this design is almost 3-times that of the planar devices and would make the reported devices highly competitive with the current best OPV devices if successfully implemented. In practice obtaining such aspect ratios as found in the interdigitated design is likely to be nontrivial in particular over large areas. One potential approach to this is through the use of nanoimprinting lithography which has previously demonstrated patterning over large areas based on low-cost DVD stamping.[20] As it can be seen in Figure 6a, even if much smaller aspect ratios (*e.g.*, 1:1) are achieved then significant improvements in device efficiency may be obtained. Recently poly(3-hexylthiophene) (P3HT):C_{60} interdigitated OPV device structures have been reported based on the use of anodic Al_2O_3 templates.[21] The template had a 100 nm period, 150 nm depth, and aspect ratio of ∼3:1 (depth/width), and the resulting devices showed a 7-fold increase in efficiency though this was achieved by increasing not only the heterojunction area but also due to an improvement in charge carrier mobility in the P3HT structures. Approaches to achieving a similar effect in hybrid amorphous silicon (*a*-Si:H)/P3HT devices has also been reported in which aspect ratios of 3:1 were also achieved for 100 nm thick *a*-Si:H films though ultimately the material combination was not successful.[22] More recently a number of advances focusing on the use of self-assembled polymers have also achieved patterning on the nanoscale in the plane of the device using block copolymers[23] and liquid crystals[24] with the later producing a structure similar to that in the model above, though with lower than optimal heights (180 nm). The ability to grow such nanostructures in an ordered way *via* the use of prepatterning a surface with a catalyst[25] to allow direct growth of nanorod organic (*e.g.*, C_{60})[26] or inorganic (*e.g.*, CdSe)[27] features may also be a feasible route.

Related to the above are efforts to further improve the exciton diffusion length in the materials systems used and charge extraction efficiency. PbS NCs are an attractive system in this regard due to their long radiative lifetime (μs)[28] and the potential for forming 1D nanowires which has received significant attention.[29−33] Of direct relevance to the above work are the demonstration of single crystal PbS nanowires with an average diameter of 50 nm and lengths typically exceeding 1000 nm *via* a chemical vapor transport (CVT) method.[32] As such, exciton diffusion lengths exceeding those typically found in organic and polymer materials are feasible and may be assisted by Förster energy transfer in ensemble systems. Alternative solution methods reported in the same publication yield similar results with diameters in the range of 20−50 nm and lengths in the range of 500−1000 nm. Such structures closely match the dimensions predicted by the 2D diffusion model as being optimal for use in OPV devices. Work on GaAs nanowires of similar dimensions have been taken a step further through their introduction into hybrid OPV devices;[33] thus, extension to PbS systems in a similar manner is feasible in the near future. Furthermore, it has been shown that nanowires have a greater absorption cross-section (∼1 order of magnitude) than NCs, which in principle could enable the high efficiencies predicted by our model to be achieved at lower values of the parameter *H*.[34]

Taking into consideration all of the above experimental advances in this fast developing field it is highly plausible that the optimal device architectures predicted by the 2D diffusion model may be realized by one of the techniques discussed or more likely a combination of them. As such the development of even more sophisticated models should be considered including those that incorporate the ability to predict the electronic characteristics of devices. The model we present represents a critical step in producing such models and guiding future experimental work.

CONCLUSIONS

The above results clearly support the rationale behind the proposition of using interdigitated heterojunction

structures to enhance the efficiency of OPV devices. Considering the wavelength dependent absorption efficiency and 2D exciton diffusion within active layers, the model provided allows optimization of the device structure to maximize the efficiency. Applied to PbS NC and C_{60} and given their full spectral response, power conversion efficiencies of 50% are achievable with the assumption of perfect charge carrier separation and collection. To reach these levels, interdigitated features with PbS NC widths of ~60 nm and C_{60} widths of ~20 nm are required with 800 nm depth. However, even for much more modest feature sizes and aspect ratios significant improvement is found over planar heterojunction devices which is expected to be common for all heterojunction forming systems in OPV devices. With the key advantage of significantly improved utilization of the near-infrared solar spectrum it is clear that semiconductor nanocrystals can play an important role in enabling the demonstration of efficient hybrid OPV devices when coupled with recent advances in nanopatterning.

METHODS

Theoretical Basis. To model the performance of single heterojunction OPV devices, two architectures were used as shown in Figure 1a. For all architectures the incident AM1.5 light intensity, $I_{AM1.5}(\lambda)$, is assumed to be normal to the ITO substrate which has a transmission coefficient $T_{ITO}(\lambda)$, both of which are shown inset to Figure 1b. First a simple bilayer device consisting of two active materials sandwiched between ITO-coated glass and Al electrode is considered, extending infinitely in the *y*- and *z*-direction. The Al top electrode was assumed to be a perfect reflector over the spectral range studied, which has a minimal impact on accuracy for the results presented here. The thickness of each layer is given as d_i with each having absorption coefficient $\alpha_i(\lambda)$ and exciton diffusion length $L_{D,i}$. In this configuration only the thickness of each of the films, d_i, is considered as a variable in the modeling where $i = 1$ (2) for the PbS NC (C_{60}) layer. The absorption coefficient of C_{60} and PbS NCs are presented in Figure 1b.

The second device architecture considered is one in which the two materials form an interdigitated structure which is repeated in the *y*-direction to form the device. The thickness of each of the two layers is the sum of the continuous layer adjacent to the electrode, d_i, and the height of the interdigitated region H, while the width of the two materials within the interdigitated region is defined as W_i. All three of these parameters were considered as variables in optimization of the device geometry.

Experimental absorption and transmission coefficients were obtained as previously reported,[7] and all modeling was undertaken using Matlab R2007b.

Acknowledgment. This work was supported by work funded *via* EPSRC Grant EP/C013824/1.

Supporting Information Available: Mathematic derivations and methods leading to the expressions used within. This material is available free of charge *via* the Internet at http://pubs.acs.org.

REFERENCES AND NOTES

1. Nielsen, T. D.; Cruickshank, C.; Foged, S.; Thorsen, J.; Krebs, F. C. Business, Market and Intellectual Property Analysis of Polymer Solar Cells. *Sol. Energy Mater. Sol. Cell.* **2010,** *94*, 1553–1571.
2. Green, M. A.; Emery, K.; Hishikawa, Y.; Warta, W. Solar Cell Efficiency Tables (Version 36). *Prog. Photovolt: Res. Appl.* **2010,** *18*, 346–352.
3. Peumans, P.; Yakimov, A.; Forrest, S. R. Small Molecular Weight Organic Thin-Film Photodetectors and Solar Cells. *J. Appl. Phys.* **2003,** *93*, 3693–3724.
4. Nelson, J.; Kirkpatrick, J.; Ravirajanm, P. Factors Limiting the Efficiency of Molecular Photovoltaic Devices. *Phys. Rev. B* **2004,** *69*, 035337.
5. McDonald, S. A.; Konstantatos, G.; Zhang, S.; Cyr, P. W.; Klem, E. J. D.; Levina, L.; Sargent, E. H. Solution-Processed PbS Quantum Dot Infrared Photodetectors and Photovoltaics. *Nat. Mater.* **2005,** *4*, 138–142.
6. Dissanayake, D. M. N. M.; Hatton, R. A.; Lutz, T.; Giusca, C. E.; Curry, R. J.; Silva, S. R. P. A PbS Nanocrystal-C_{60} Photovoltaic Device for Infrared Light Harvesting. *Appl. Phys. Lett.* **2007,** *91*, 133506.
7. Dissanayake, D. M. N. M.; Hatton, R. A.; Lutz, T.; Curry, R. J.; Silva, S. R. P. The Fabrication and Analysis of a PbS Nanocrystal:C_{60} Bilayer Hybrid Photovoltaic System. *Nanotechnology* **2009,** *20*, 245202.
8. Seo, J.; Kim, S. J.; Kim, W. J.; Singh, R.; Samoc, M.; Cartwright, A. N.; Prasad, P. N. Enhancement of the Photovoltaic Performance in PbS Nanocrystal:P3HT Hybrid Composite Devices by Post-Treatment-Driven Ligand Exchange. *Nanotechnology* **2009,** *20*, 095202.
9. Tsang, S. W.; Fu, H.; Wang, R.; Lu, J.; Yu, K.; Tao, Y. Highly Efficient Cross-Linked PbS Nanocrystal/C_{60} Hybrid Heterojunction Photovoltaic Cells. *Appl. Phys. Lett.* **2009,** *95*, 183505.
10. Nicholson, P. G.; Castro, F. A. Organic Photovoltaics: Principles and Techniques for Nanometre Scale Characterization. *Nanotechnology* **2010,** *21*, 492001.
11. Deibel, C.; Dyakonov, V. Polymer–Fullerene Bulk Heterojunction Solar Cells. *Rep. Prog. Phys.* **2010,** *73*, 096401.
12. Martin, C. M.; Burlakov, V. M.; Assender, H. E.; Barkhouse, D. A. R. A Numerical Model for Explaining the Role of the Interface Morphology in Composite Solar Cells. *J. Appl. Phys.* **2007,** *102*, 104506.
13. Williams, J.; Walker, A. B. Two-Dimensional Simulations of Bulk Heterojunction Solar Cell Characteristics. *Nanotechnology* **2008,** *19*, 424011.
14. Stubinger, T.; Brutting, W. Exciton Diffusion and Optical Interference in Organic Donor–Acceptor Photovoltaic Cells. *J. Appl. Phys.* **2001,** *90*, 3632–3641.
15. Tenenbaum, M.; Pollard, H. *Ordinary Di□erential Equations*; Dover Publications; Mineola, New York, 1985.
16. Luther, J. M.; Law, M.; Beard, M. C.; Song, Q.; Reese, M. O.; Ellingson, R. J.; Nozik, A. J. Schottky Solar Cells Based on Colloidal Nanocrystals Films. *Nano Lett.* **2008,** *8*, 3488–3492.
17. Szendrei, K.; Gomulya, W.; Yarema, M.; Hieww, W.; Loi, M. A. PbS Nanocrystal Solar Cells with High Efficiency and Fill Factor. *Appl. Phys. Lett.* **2010,** *97*, 203501.
18. Choi, J. J.; Lim, Y.; M. Santiago-Berrios, B.; Oh, M.; Hyun, B.; Sun, L.; Bartnik, A. C.; Goedhart, A.; Malliaras, G. G.; Abruna, H. D.; *et al.* PbSe Nanocrystal Excitonic Solar Cells. *Nano Lett.* **2009,** *9*, 3749–3755.
19. Press, W. H.; Teukolsky, S. A.; Vetterling, W. T.; Flannery, B. P. *Numerical Recipes, The Art of Scientific Computing*; Cambridge University Press: Cambridge, 2007; pp 1024–1083.
20. Emah, J. B.; Curry, R. J.; Silva, S. R. P. Low Cost Patterning of Poly(3,4-ethylenedioxythiophene Poly(styrenesulfonate)

Films To Increase Organic Photovoltaic Device Efficiency. *Appl. Phys. Lett.* **2008,** *93*, 103301.
21. Kim, J. S.; Park, Y.; Lee, D. Y.; Lee, J. H.; Park, J. H.; Kim, J. K.; Cho, K. Poly(3-hexylthiophene) Nanorods with Aligned Chain Orientation for Organic Photovoltaics. *Adv. Funct. Mater.* **2010,** *20*, 540–545.
22. Gowrishankar, V.; Scully, S. R.; Chan, A. T.; McGehee, M. D.; Wang, Q.; Branz, H. M. Exciton Harvesting, Charge Transfer and Carrier Transport in Amorphous-Silicon Nanopillar/Polymer Hybrid Solar Cells. *J. Appl. Phys.* **2008,** *103*, 064511.
23. Tseng, Y.; Darling, S. B. Block Copolymer Nanostructures for Technology. *Polymers* **2010,** *2*, 470–489.
24. Hesse, H. C.; Lembke, D.; Dossel, L.; Feng, X.; Mullen, K.; Schmidt-Mende, L. Nanostructuring Discotic Molecules on ITO Support. *Nanotechnology* **2011,** *22*, 055303.
25. Mizuno, H.; Buriak, J. M. Building Upon Patterned Organic Monolayers Produced *via* Catalytic Stamp Lithography. *ACS Appl. Mater. Interfaces* **2010,** *2*, 2301–2307.
26. Chong, L. C.; Sloan, J.; Wagner, G.; Silva, S. R. P.; Curry, R. J. Controlled Growth of True Nanoscale Crystal Fullerites for Device Applications. *J. Mater. Chem.* **2008,** *18*, 3319–3324.
27. McClure, S. A.; Worfolk, B. J.; Rider, D. A.; Tucker, R. T.; Fordyce, J. A. M.; Fleischauer, M. D.; Harris, K. D.; Brett, M. J.; Buriak, J. M. Electrostatic Layer-by-Layer Assembly of CdSe Nanorod/Polymer Nanocomposite Thin Films. *ACS Appl. Mater. Interfaces* **2010,** *2*, 2219–229.
28. Nordin, M. N.; Bourdakos, K. N.; Curry, R. J. Charge Transfer in Hybrid Organic–Inorganic PbS Nanocrystal Systems. *Phys. Chem. Chem. Phys.* **2010,** *12*, 7371–7377.
29. Chen, J.; Vhen, L.; Wu, L. The Solventless Synthesis of Unique PbS Nanowires of X-Shaped Cross Sections and the Cooperative Effects of Ethylenediamine and a Second Salt. *Inorg. Chem.* **2007,** *46*, 8038–8043.
30. Talapin, D. V.; Yu, H.; Shevchenko, E. V.; Lobo, A.; Murray, C. B. Synthesis of Colloidal PbSe/PbS Core–Shell Nanowires and PbS/Au Nanowire–Nanocrystal Heterostructures. *J. Phys. Chem. C* **2007,** *111*, 14049–14054.
31. Lau, Y. K. A.; Chernak, D. J.; Bierman, M. J.; Jin, S. Formation of PbS Nanowire Pine Trees Driven by Screw Dislocations. *J. Am. Chem. Soc.* **2009,** *131*, 16461–16471.
32. Jang, Y.; Song, Y. M.; Kim, H. S.; Cho, Y. J.; Seo, Y. S.; Jung, G. B.; Lee, C.; Park, J.; Yung, M.; Kim, J.; *et al*. Three Synthetic Routes to Single-Crystalline, PbS Nanowires with Controlled Growth Direction and Their Electrical Transport Properties. *ACS Nano* **2010,** *4*, 2391–2400.
33. Ren, S.; Zhao, N.; Crawford, S. C.; Tambe, M.; Bulovic, V.; Gradecak, S. Heterojunction Photovoltaics Using GaAs Nanowires and Conjugated Polymers. *Nano Lett.* **2010,** *11*, 408–413.
34. Giblin, J.; Kuno, M. Nanostructure Absorption: A Comparative Study of Nanowire and Colliodal Quantum Dot Absorption Cross Sections. *J. Phys. Chem.* **2010,** *1*, 3340–3348.